



The local disorder induced by high-entropy doping results in highly stable cathode materials for aqueous potassium-ion batteries

Guowei Zeng^a, Bingqiu Liu^{a,*}, Usman Ali^a, Yanxin Li^a, Hongfeng Jia^a, Maoyu Sun^a, Yiqian Li^a, Yuehan Hao^a, Xue Yong^c, Tingting Wang^{b,*}, Chungang Wang^{a,*}

^a Country Faculty of Chemistry of Northeast Normal University of China, Changchun 130024, PR China

^b School of Chemistry & Environmental Engineering of Changchun University of Science and Technology, Changchun 130022, PR China

^c University of Sheffield, department of chemistry

ARTICLE INFO

Keywords:

High-entropy doping
Aqueous potassium ion batteries
Layered manganese-based oxides
Local disorder

ABSTRACT

Aqueous potassium-ion batteries are poised to become leading candidates for next-generation large-scale storage technology due to their low cost and safety features. However, the stability of aqueous potassium-ion battery materials faces significant challenges. The large ionic radius of potassium ions causes significant stress changes in the ordered crystal structure of the materials during the charge-discharge process. To address this issue, we synthesized high-entropy-doped layered manganese oxide (HE-KMO). High-entropy doping reconstructed the electron cloud distribution between the layers of HE-KMO, causing local disorder in HE-KMO. Local disorder reduces the transport barrier by inducing the transport of potassium ions and alleviates the stress on the material. It prevented phase transitions of HE-KMO during charging and discharging, improving the stability of HE-KMO. We used HE-KMO in the cathode material of aqueous potassium-ion batteries. Under a current of 5 A g⁻¹, HE-KMO maintains an outstanding capacity retention after 5000 cycles.

1. Introduction

Clean energy has been gaining more and more attention in recent years. Rechargeable secondary batteries are essential for integrating renewable energies like wind, solar, and tidal power [1–8]. Current batteries face limitations in large-scale energy storage (ESS) due to factors like flammable electrolytes [9,10]. Aqueous batteries offer a promising solution to these problems due to their ease of manufacturing, low cost, and increased ion mobility [11,12]. Among various aqueous batteries, aqueous potassium-ion batteries (AKIBs) have attracted widespread attention. Potassium ions have high natural abundance and relatively small hydration radii, making AKIBs promising for lower costs and faster ion migration rates [13–16]. AKIBs are expected to be candidates for the large-scale energy storage technologies [17–20]. However, the larger ionic radius of potassium ions presents serious challenges to the material in various aspects when embedded [21–23]. In terms of stability, most current aqueous potassium ion materials experience significant stress changes during potassium extraction and insertion, leading to rapid degradation of material performance. On the other hand, the large radius of potassium ions also significantly affects

the transmission speed of potassium ions in the material. Therefore, how to address the challenges of large-radius potassium ion insertion is a primary issue in aqueous potassium-ion batteries [24–26].

Recently, new insights have been proposed for this problem through the method of inducing ion transport by local disorder. Chen et al. enhanced the speed of potassium ion insertion into materials by forming a local disordered structure in TiO₂ materials [27]. Cai et al. successfully synthesized Li_{1.2}Ni_{0.2}Mn_{0.6}O₂ materials with different amounts of structural defects using powder metallurgy technology, where the disorder of the transition metal layer promoted the stability of their materials [28]. The local disorder can greatly improve the material affected by ion insertion. Specifically, the disordered distribution of local electron clouds can induce the location of ion insertion, thereby mitigating the intense stress changes that the overall active material undergoes during the cycling process [29–31]. In addition, local disorder can reduce the ion insertion barrier at specific sites, allowing ions to be inserted and deintercalated faster [32,33]. For aqueous potassium-ion batteries troubled by the large radius of potassium ions, inducing the transport of potassium ions through local disorder may be a potential solution to this problem. However, the construction of materials with

* Corresponding authors.

E-mail addresses: liubq142@nenu.edu.cn (B. Liu), wangcg925@nenu.edu.cn (C. Wang).

<https://doi.org/10.1016/j.apcatb.2024.123996>

Received 4 January 2024; Received in revised form 3 March 2024; Accepted 20 March 2024

Available online 21 March 2024

0926-3373/© 2024 Elsevier B.V. All rights reserved.

local disorder is not very controllable, making it difficult for mass production.

High-entropy materials are a new class of materials composed of multiple components. High-entropy materials generally have the characteristic of convenient synthesis. Moreover, high-entropy materials can cause local disorder by introducing multiple different elements. Therefore, high-entropy materials generally have high stability [34,35]. However, the traditional near-equal molar high-entropy strategy has been proven to reduce the reversible capacity of the material [36–38]. To introduce local disorder and avoid the capacity reduction caused by traditional high-entropy doping, we noticed the strategy of complex component doping (high-entropy doping). We hope to induce local disorder in the material by substituting a minor amount of active elements, enabling the material to not only retain its capacity but also effectively mitigate the stress within the material's crystal structure during the cycling process, preventing material dissolution and thus stabilizing the material's overall structure [39]. Therefore, we propose that the implementation of local disorder via a high-entropy doping strategy can suppress material dissolution and achieve highly stable aqueous potassium ion cathode materials.

In this work, we doped Fe, Co, Ni, Zn and Mg elements into layered manganese-based oxides (LMO), synthesizing layered manganese-based oxides (HE-KMO) with high-entropy doping. The uneven distribution of electron clouds among various elements causes HE-KMO to produce local disorder, which induces the embedding of potassium ions and reduces the severe stress changes experienced by the active material during the cycle. We used HE-KMO in the cathode material of aqueous potassium ion batteries, and HE-KMO showed excellent performance. After 500 cycles, HE-KMO maintained a capacity retention rate close to 100%, better than the 48.6% capacity retention rate of ordinary KMO materials. This indicates that introducing local disorder through the high-entropy doping strategy can induce the embedding of potassium ions and greatly improve the stability of the material. This provides new insights for finding new high-stability materials for aqueous potassium-ion batteries.

2. Experiment

2.1. Materials

The materials utilized in this study are detailed in the [Supporting Information](#). (Text S1)

2.2. Synthesis methods

2.2.1. Synthesis of KMO

4.5 mmol of $\text{MnCl}_2 \cdot 4 \text{H}_2\text{O}$, 2 g of KNO_3 and 1 g of citric acid were added to 30 ml of deionized water and the deionized water was evaporated to dryness at 100 °C. The resulting powder was burned in air at 800 °C for 30 minutes. Subsequently, the obtained material was rinsed with deionized water and centrifuged. Finally, it was left in an oven at 50 °C for 20 hours.

2.2.2. Synthesis of HE-KMO

4.5 mmol of $\text{MnCl}_2 \cdot 4 \text{H}_2\text{O}$, 0.1 mmol of $\text{Fe}(\text{NO}_3)_3$, 0.1 mmol of $\text{Co}(\text{NO}_3)_2$, 0.1 mmol of $\text{Ni}(\text{NO}_3)_2$, 0.1 mmol of $\text{Zn}(\text{NO}_3)_2$, 0.1 mmol of $\text{Mg}(\text{NO}_3)_2$, 2 g of KNO_3 and 1 g of citric acid were added to 30 ml of deionized water and the deionized water was evaporated to dryness at 100 °C. The resulting powder was burned in air at 800 °C for 30 minutes. Subsequently, the obtained material was rinsed with deionized water and centrifuged. Finally, it was left in an oven at 50 °C for 20 hours.

2.2.3. Synthesis of HE-KMO-1

4 mmol of $\text{MnCl}_2 \cdot 4 \text{H}_2\text{O}$, 0.2 mmol of $\text{Fe}(\text{NO}_3)_3$, 0.2 mmol of $\text{Co}(\text{NO}_3)_2$, 0.2 mmol of $\text{Ni}(\text{NO}_3)_2$, 0.2 mmol of $\text{Zn}(\text{NO}_3)_2$, 0.2 mmol of $\text{Mg}(\text{NO}_3)_2$, 2 g of KNO_3 and 1 g of citric acid were added to 30 ml of

deionized water and the deionized water was evaporated to dryness at 100 °C. The resulting powder was burned in air at 800 °C for 30 minutes. Subsequently, the obtained material was rinsed with deionized water and centrifuged. Finally, it was left in an oven at 50 °C for 20 hours.

2.2.4. Synthesis of HE-KMO-2

1 mmol of $\text{MnCl}_2 \cdot 4 \text{H}_2\text{O}$, 1 mmol of $\text{Fe}(\text{NO}_3)_3$, 1 mmol of $\text{Co}(\text{NO}_3)_2$, 1 mmol of $\text{Ni}(\text{NO}_3)_2$, 1 mmol of $\text{Zn}(\text{NO}_3)_2$, 1 mmol of $\text{Mg}(\text{NO}_3)_2$, 2 g of KNO_3 and 1 g of citric acid were added to 30 ml of deionized water and the deionized water was evaporated to dryness at 100 °C. The resulting powder was burned in air at 800 °C for 30 minutes. Subsequently, the obtained material was rinsed with deionized water and centrifuged. Finally, it was left in an oven at 50 °C for 20 hours.

2.2.5. Synthesis of M-KMO (M=Ni, Co, Fe, Zn, Mg)

4.5 mmol of $\text{MnCl}_2 \cdot 4 \text{H}_2\text{O}$, 0.5 mmol of $\text{M}(\text{NO}_3)_3$ (M=Ni, Co, Fe, Zn, Mg), 2 g of KNO_3 and 1 g of citric acid were added to 30 ml of deionized water and the deionized water was evaporated to dryness at 100 °C. The resulting powder was burned in air at 800 °C for 30 minutes. Subsequently, the obtained material was rinsed with deionized water and centrifuged. Finally, it was left in an oven at 50 °C for 20 hours.

2.3. Characterization

Specific characterizations are detailed in the [Supporting Information](#). (Text S2)

2.4. Electrochemical tests

Specific electrochemical tests are detailed in the [supporting information](#). (Text S3)

2.5. Computational methods

Specific computational methods are detailed in the [supporting information](#). (Text S4)

3. Results and discussion

3.1. Structural characterization of materials

Using the sole gel method, we synthesized KMO and HE-KMO. Rietveld refinement analysis was conducted on the X-ray diffraction (XRD) patterns of KMO and HE-KMO, respectively (Fig. 1a and Fig. S2). The XRD results reveal that KMO aligns with the C/2 m structure within the space group, mirroring the lattice structure of $\text{K}_{0.46}\text{Mn}_2\text{O}_4 \cdot 1.6 \text{H}_2\text{O}$. For HE-KMO, all diffraction peaks can be indexed as an R-3 m structure, corresponding to the lattice structure of $\text{K}_{0.27}\text{Mn}_2\text{O}_5 \cdot 0.54 \text{H}_2\text{O}$. The crystal structures of KMO and HE-KMO are shown in Fig. 1b and Fig. 1c. Doped ions occupy the octahedral sites of Mn, with K situated between the two adjacent TMO_2 layers. Compared to the neatly arranged KMO, HE-KMO becomes more disordered in its lattice due to the sites of Mn being replaced by different elements. The long-range order present in KMO disappears in HE-KMO, making HE-KMO locally disordered. By scanning electron microscopy (SEM) and high-resolution transmission (TEM), We found that HE-KMO and KMO have an irregular blocky morphology (Fig. 1d, f and Fig. S3). The lattice stripes of HE-KMO show a very high crystallinity (Fig. 1e), which is consistent with the XRD pattern. The TEM elemental mappings illustrate a uniform distribution of all elements throughout the material (Fig. 1g). We used inductively coupled plasma (ICP) to test the specific elemental ratios in the material (Table S1), with each element in HE-KMO having a content close to 2%, which suggests that all cations are doped into the lattice. The ratio of Mn to K is also close to that of $\text{K}_{0.27}\text{Mn}_2\text{O}_5$, so we named our synthesized HE-KMO as $\text{K}_{0.27}\text{Mn}_{0.9}(\text{Fe}_{0.02}\text{Co}_{0.02}\text{Ni}_{0.02}\text{Zn}_{0.02}\text{Mg}_{0.02})\text{O}_2$.

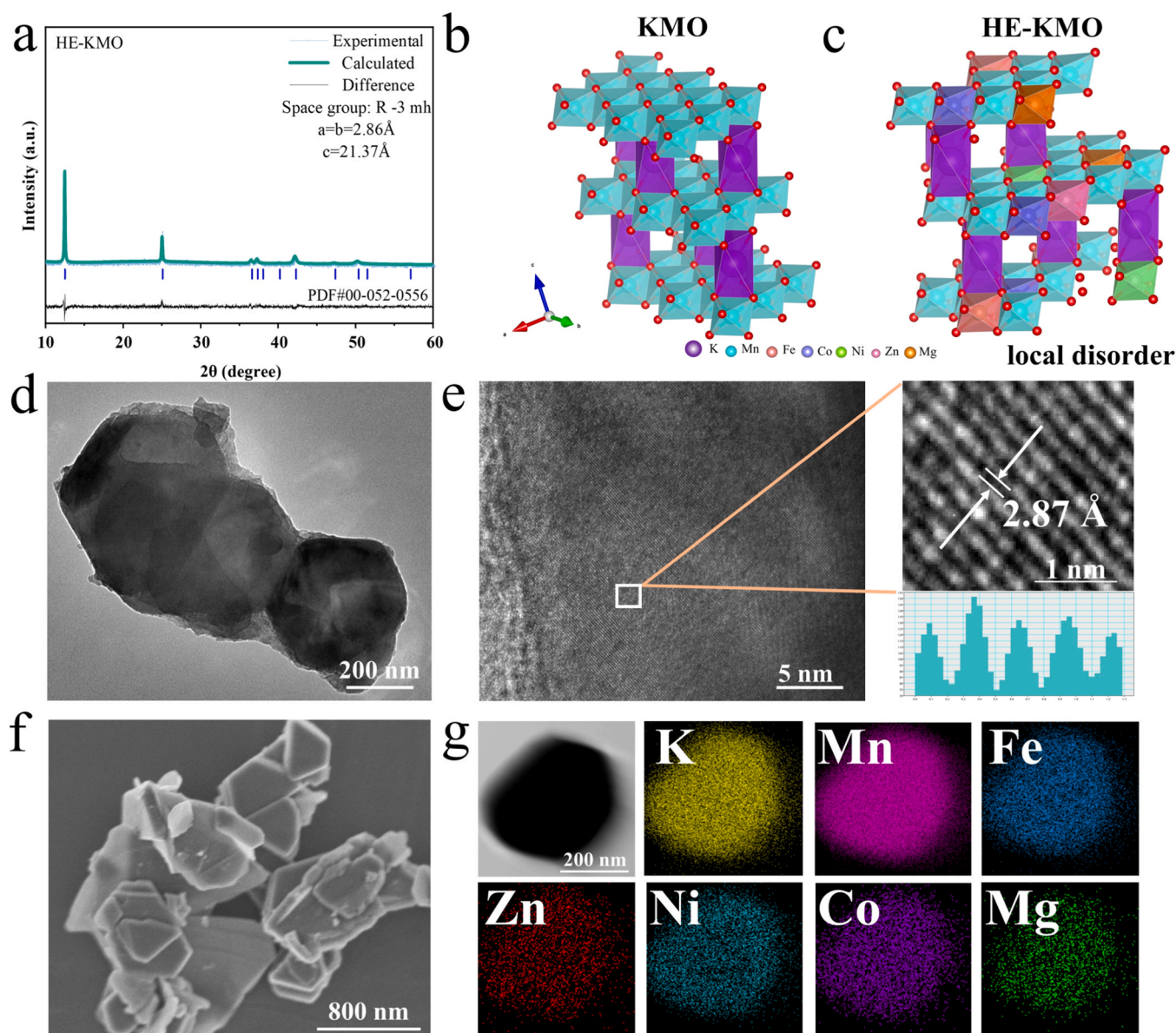


Fig. 1. (a) XRD refined patterns of HE-KMO. (b, c) Schematic diagram of the lattice structure of KMO and HE-KMO. (d, e) Transmission electron microscopy images of HE-KMO. (f) Scanning electron microscopy image of HE-KMO. (g) Elemental mappings of HE-KMO.

3.2. Electrochemical characterization

We examined the electrochemical properties of KMO and HE-KMO. KMO shows two redox peaks at scan rates of $1\text{--}5\text{ mV s}^{-1}$ (Fig. 2a), possibly suggesting a two-step reaction for potassium ions intercalation into KMO. However, HE-KMO retains only one redox peak (Fig. 2b), and the peak broadens. We employed the formula $i = a \cdot v^b$ to analyze the CV curves of KMO and HE-KMO (Fig. 2c). The calculated b value for HE-KMO is closer to 1 compared to KMO, indicating that surface-controlled electrochemical kinetic process governs the kinetics of the HE-KMO. This is also corroborated by the pseudocapacitive contribution ratio plot (Figs. 2d, 2e). HE-KMO has a higher pseudocapacitive contribution ratio than the KMO pseudocapacitive contribution ratio (Fig. S7). This may be related to the local disorder caused by doping, which leads to changes in the lattice energy barrier and electron cloud distribution, resulting in a change in the intercalation way of potassium ions. To compare the difference between single-element doping and high-entropy doping, we also synthesized layered potassium manganese oxides doped with individual elements (M-KMO, where $M = \text{Ni, Fe, Co,}$

Mg, Zn) and their XRD patterns are shown in Fig. S4. We conducted pseudocapacitive contribution analysis on M-KMO ($M = \text{Ni, Fe, Co, Mg, Zn}$) (Fig. S6 a-e). The results show that the local disorder caused by doping will lead to varying degrees of increase in the contribution of pseudocapacitance. To further elucidate the effect of high-entropy doping on electrochemical properties, we compared the 1 mV s^{-1} CV curves of M-KMO and HE-KMO (Fig. 2f). The redox peak positions of different M-KMO vary due to the effect of doped elements, and the broader redox peak of HE-KMO might result from the merging of redox peaks caused by the high-entropy effect [40]. Moreover, The reduction peak of HE-KMO shifts to a higher voltage compared to KMO, which is similar to previous reports [41], indicating that the synergistic effect of high entropy can increase the oxidation potential of Mn. We employed electrochemical impedance spectroscopy to investigate the charge transfer rate at the electrode-electrolyte interface (Fig. 2g). Compared to KMO, HE-KMO has a smaller semicircle diameter. We further used the galvanostatic intermittent titration technique (GITT) to test the diffusion kinetics of K^+ (Fig. 2h, i). As observed, HE-KMO has a faster K^+ diffusion rate than KMO. The reason why HE-KMO can intercalate and

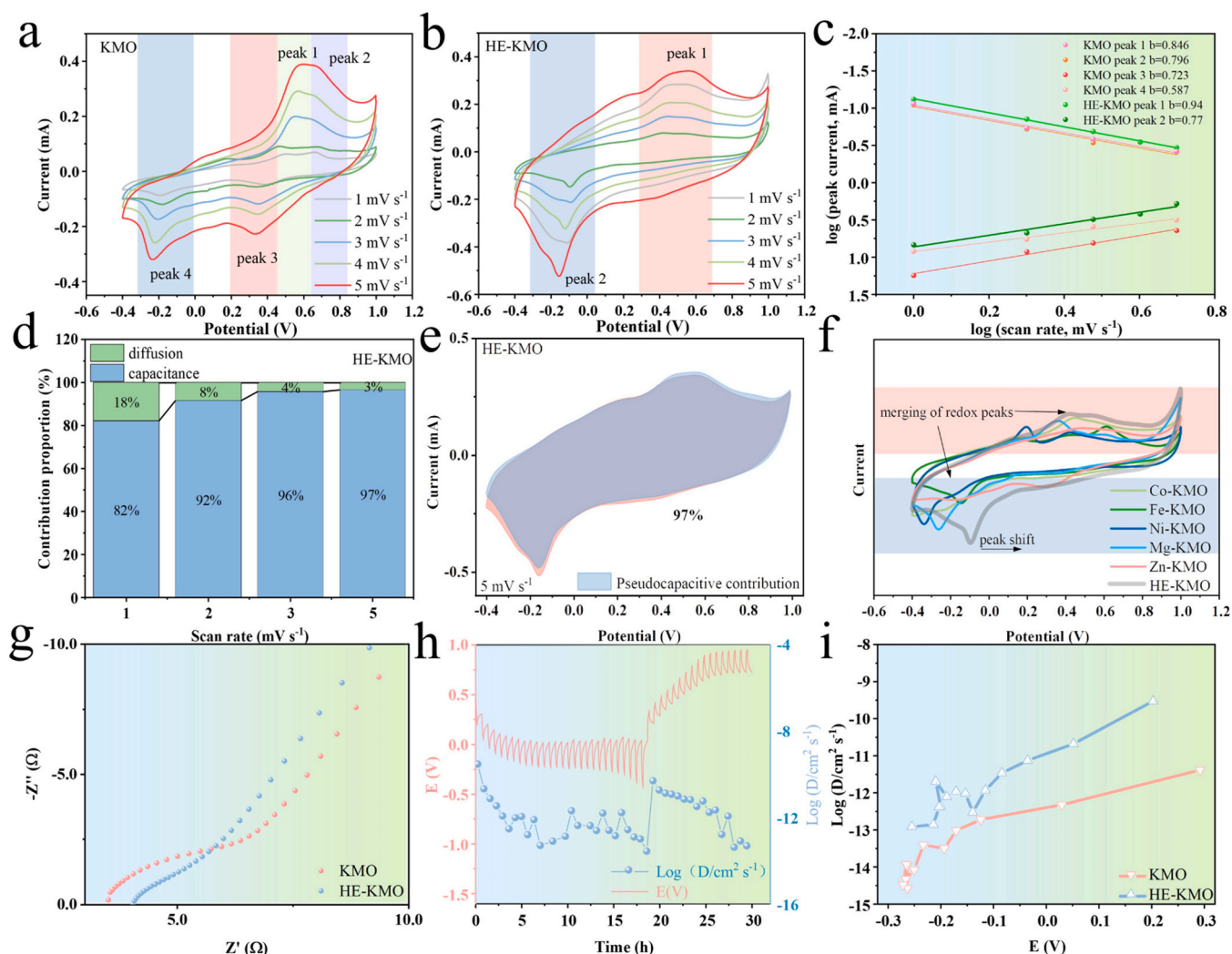


Fig. 2. CV curves of KMO (a) and HE-KMO (b) from 1–5 mV s^{-1} . (c) $\log(\text{peak current})$ – $\log(\text{scan rate})$ curves for different plateaus. (d) The distribution of pseudocapacitive contributions and diffusive behaviours across different scan rates is analysed. (e) Pseudocapacitive contribution at 5 mV s^{-1} . (f) Comparison of CV curves of HE-KMO and M-KMO (M=Ni, Co, Fe, Zn, Mg). (g) Nyquist plots of KMO and HE-KMO. (h) The galvanostatic intermittent titration technique (GITT) curves for HE-KMO. (i) The K-ion diffusion coefficient for KMO and HE-KMO.

deintercalate K^+ more quickly may be due to the local disorder induced by high-entropy doping. By regulating K^+ , it allows K^+ to transmit at lower energy barrier positions, thereby accelerating the diffusion speed of potassium ions.

3.3. Electrochemical performance of HE-KMO and KMO

We conducted charge-discharge tests on the materials in a three-electrode system. It is interesting to note that there are notable differences between the discharge curve of HE-KMO and the discharge curve of KMO (Fig. 3a). KMO has two plateaus, around 0.4 V and –0.3 V, which is consistent with the results of the CV curve. The plateau at 0.4 V contributes around 10% of the specific capacity, while the second plateau below –0.2 V accounts for 42% of the specific capacity. In the case of HE-KMO, the two plateaus merge into a single plateau at 0 V. Relative to KMO, HE-KMO delivers 73% of the total capacity at voltages above –0.2 V. In comparison, HE-KMO can provide more capacity at higher voltages. We evaluated the rate performance of KMO and HE-KMO (Fig. 3d); at a current density of 5 A g^{-1} , HE-KMO exhibited a specific capacity of 69 mAh g^{-1} . Upon reducing the current back to 1 A g^{-1} , HE-KMO's capacity restored to approximately 90 mAh g^{-1} . This indicates that HE-KMO has a good rate performance and stability.

Furthermore, HE-KMO can provide a specific capacity of 90 mAh g^{-1} , which is higher than the 77 mAh g^{-1} of KMO. The capacity enhancement can be attributed to the complementary promotion of high-entropy doped ions and potassium ions, facilitating the migration of K^+ [42]. We conducted EPR tests on two materials and found that HE-KMO has a higher level of oxygen vacancies (Fig. S8), which suggests the local disorder generated by high-entropy doping provides more active sites for potassium ions [43]. Fig. 3b and Fig. 3c show the charge-discharge curves of HE-KMO and KMO for the first 100 cycles. The capacity retention rate of KMO in the first 100 cycles is only 71%, and rapid decay of the 0.4 V plateau can be observed in the figure, which may be related to the phase transition that occurs during potassium ion insertion in KMO. Conversely, HE-KMO exhibits a slight capacity increase during the initial 100 cycles, with a minor elevation and expansion of the plateau, which is related to the activation of manganese-based oxide materials [44,45]. We tested the stability of HE-KMO and KMO (Fig. 3e). KMO dissolved after 500 cycles, retaining only 48.6% of its capacity, while HE-KMO still maintained close to 100% capacity. During the test, we monitored the Mn content in the electrolyte (Fig. 3f). At the 500th cycle, the dissolved Mn content in the KMO electrolyte was 9.3%, much higher than the 2.7% in HE-KMO. This indicates that the structure of KMO was damaged during cycling, leading to the dissolution of Mn ions. To better

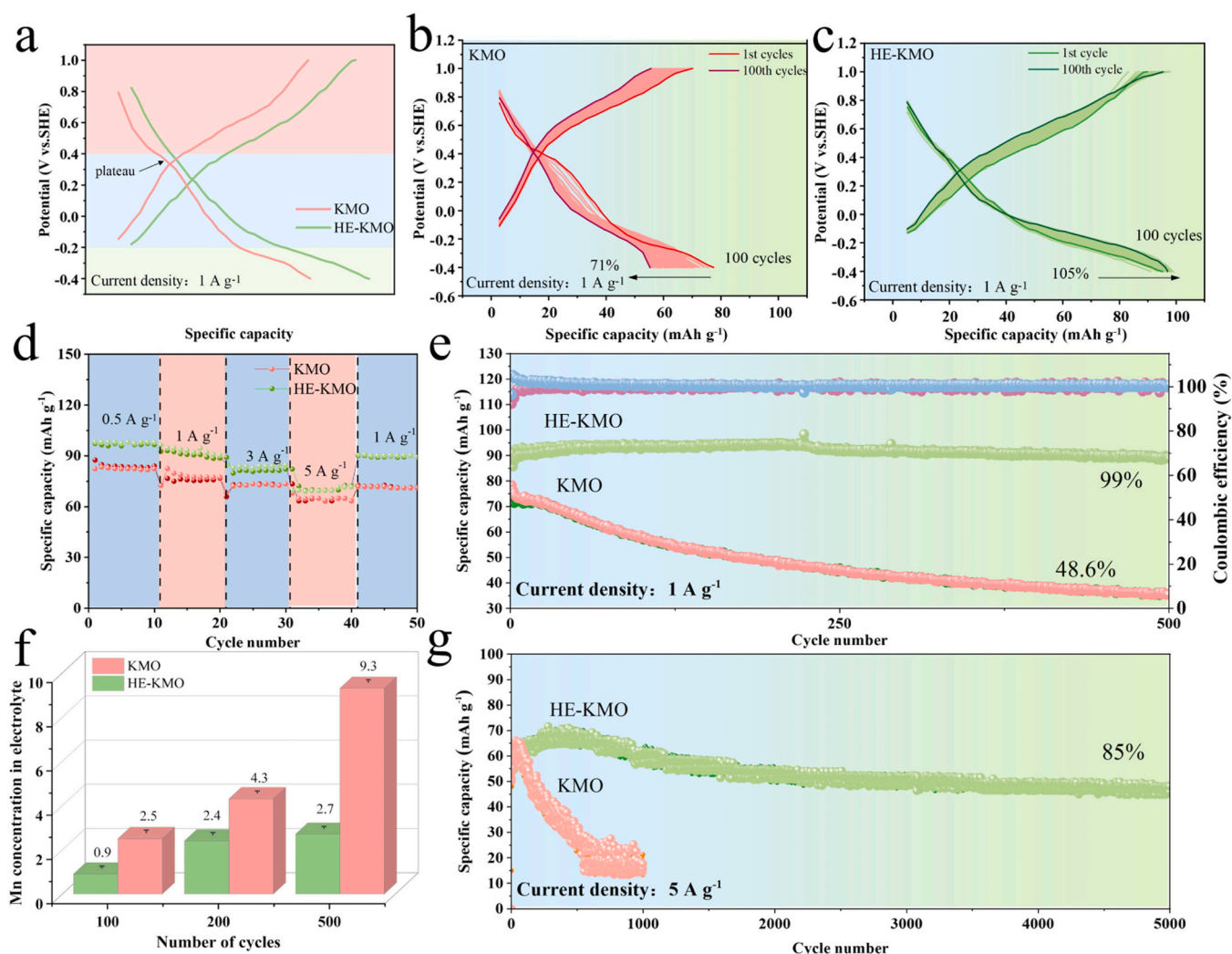


Fig. 3. (a) Charge-discharge curves of KMO and HE-KMO at a current density of 1 A g^{-1} . (b, c) KMO and HE-KMO charge-discharge curves for the first 100 cycles at 1 A g^{-1} . (d) Rate capability of KMO and HE-KMO from 0.5 to 5 A g^{-1} . (e) KMO and HE-KMO cycling stability for 500 cycles at 1 A g^{-1} current density. (f) Mn concentration percentages of KMO and HE-KMO in $1 \text{ M CH}_3\text{COOK}$ electrolyte at the 100th, 200th, and 500th cycles. (g) Long cycling stability of KMO and HE-KMO at 5 A g^{-1} current density.

illustrate this discrepancy, we employed an optical camera to compare the conditions of the two electrolyte groups (Fig. S9). We observed that the KMO electrolyte notably turned yellow brown with some precipitation, while HE-KMO maintained its colorless transparency. Furthermore, we compared the SEM images of HE-KMO and KMO after 100 cycles in 1 M KAC (Fig. S10). We found that the surface of HE-KMO did not show significant changes compared to its initial state, whereas KMO exhibited surface fracturing after 100 cycles, which is related to material dissolution. This indicates that HE-KMO has better structural stability, and the high-entropy doping strategy successfully suppressed the dissolution of HE-KMO during cycling. We subsequently conducted long-cycle tests on HE-KMO and KMO at a high current of 5 A g^{-1} (Fig. 3g). The capacity of KMO drops sharply after 600 cycles, indicating that the structure of KMO is quickly destroyed under a current of 5 A g^{-1} . Correspondingly, even after 5000 cycles, HE-KMO maintains 85% of its specific capacity. The above results indicate that high-entropy doping can greatly improve the structural stability of KMO.

We further explored higher doping concentrations and discovered that increased doping levels result in the emergence of mixed phases and a decrease in specific capacity (Fig. S11). Specifically, the amount of elemental doping in HE-KMO-1 is twice that of HE-KMO; in HE-KMO-2, we conducted proportional doping. The XRD patterns of these samples

are shown in Fig. S11a. The XRD pattern of HE-KMO-1 is similar to that of HE-KMO, but there is a mixed peak around 30° resembling Mn_3O_4 . The XRD pattern of HE-KMO-2 displays a clear Mn_3O_4 structure. We conducted battery tests on HE-KMO-1, which showed lower capacity and poorer stability. This suggests that excessive doping does not make the material structure more stable; on the contrary, it results in the production of by-products from other phases, thereby reducing the material's performance. We additionally compared the cycling performance of M-KMO ($\text{M} = \text{Ni}, \text{Fe}, \text{Co}, \text{Mg}, \text{Zn}$), proving that high-entropy doping is more effective in preserving structural stability. (Fig. S12)

3.4. Mechanistic characterization of potassium ion storage

To delve deeper into the reasons behind the superior stability of HE-KMO, we investigated the specific changes of HE-KMO and KMO during the charge-discharge process using in-situ XRD techniques (Fig. 4a, b). For HE-KMO (Fig. 4a), its characteristic peak slightly shifts to the right with the insertion of potassium ions. This increase is attributable to the enhanced electrostatic repulsion between adjacent oxygen layers following the removal of K^+ , which leads to an expanded interlayer distance [46]. As for the reaction of KMO, during the charge-discharge process, there is a significant peak transition around 40° . This can be

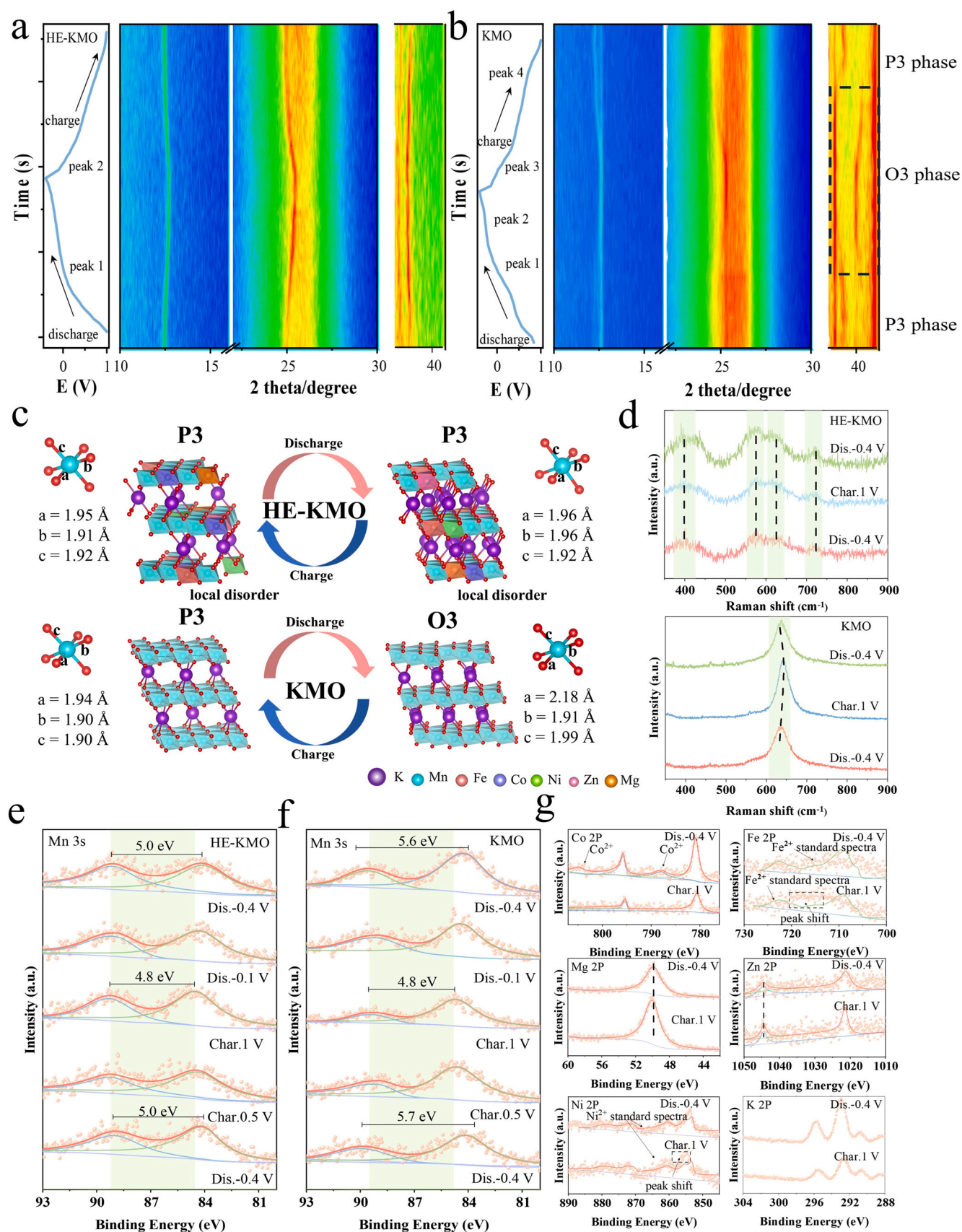


Fig. 4. (a, b) In-situ XRD patterns of HE-KMO and KMO during charge-discharge processes. (c) Schematic illustration of potassium ion intercalation and deintercalation in HE-KMO and KMO. (d) Raman spectra of HE-KMO and KMO during charge-discharge processes. (e, f) XPS Mn 3s spectra of HE-KMO and KMO during charge-discharge processes. (g) XPS spectra of Ni, Fe, Co, Mg, Zn, and K in HE-KMO during charge and discharge processes.

attributed to the transition from the O3 phase to the P3 phase [47]. According to previous reports, the change from O3 to P3 causes a significant volume change, leading to the degradation of material performance [48]. O3-P3 phase transitions can be due to changes in interlayer electrostatic repulsion in de-potassiation and potassiation processes [49]. The absence of phase transition in HE-KMO may be due to the local disorder reducing the stress changes during the material cycling process by inducing the transport of potassium ions. Based on the XRD pattern, we constructed schematic diagrams of the crystal cell structures of KMO and HE-KMO during the potassium ion deintercalation process (Fig. 4c): HE-KMO does not undergo phase transitions during the charging and discharging process, always maintaining the P3 phase, while KMO undergoes a phase transition from O3 to P3 during the charging process. We calculated the changes in the axial length of the MO_6 octahedron during the charging and discharging process through theoretical calculations. As there is no phase transition in HE-KMO during the charge-discharge process, the MO_6 octahedral structure maintains stability. However, the lengths of the *a* and *c* axes in the MO_6 octahedral structure of KMO undergo significant changes. The MO_6 octahedron of KMO suffers unstable asymmetric expansion, and contraction will lead to structural disruption [50]. For HE-KMO, it undergoes a strain-free solid solution reaction during the charging/discharging process. We further verified this point with the Raman spectrum (Fig. 4d). We have examined the Raman spectra of both HE-KMO and KMO during charging and discharging. Due to the presence of only Mn-O bonds in KMO, a strong signal peak is displayed at 638 cm^{-1} . In the de-potassiation and potassiation processes, the Raman peak of KMO evidently shifted, associated with Mn-O bond stretching, suggesting significant MnO_6 octahedral changes. For HE-KMO, due to the effect of high-entropy doping, different spectral peaks appeared, which can be attributed to Zn-O, Fe-O, Ni-O, Co-O, and Mg-O bonds. We observed the Mn-O peak broadening around 638 cm^{-1} , which demonstrates that high-entropy doping effectively impacts Mn-O bonds. We compared the Raman peaks of HE-KMO and found that the positions were essentially consistent, indicating that MnO_6 octahedral remains stable during de-potassiation and potassiation processes due to the synergistic effect of high-entropy doping. This is consistent with XRD results. XPS can elucidate the charge state of the material surface, and we explored the XPS spectra of Mn in HE-KMO and KMO during charging and discharging (Fig. 4 e, f). The distance between two peaks in Mn 3s often represents Mn valence states. When the Mn is +4 valence, the standard distance between the two peaks in Mn 3s is 4.8 eV; when the Mn is +3 valence, this value becomes 5.5 eV. In the charging and discharging process, the distance between the two peaks in KMO expands from 4.8 eV to 5.7 eV, suggesting that the Mn on the KMO surface essentially becomes +3 valence. The distance between the two peaks in HE-KMO merely expands from 4.8 eV to 5.0 eV, indicating that the valence of Mn in HE-KMO remains essentially stable. Such small changes can be attributed to the cooperative effect of high-entropy doping, and we investigated the changes of various elements during the charge-discharge process (Fig. 4 g). Among them, Fe, Co, and Ni undergo peak shifts due to their easy valence change; Mg and Zn do not shift due to their stable valence bonds, but their half-peak widths change significantly, indicating that the electron cloud distribution of Mg and Zn has changed. The XPS spectra of various elements show that all elements participate in electron reactions, resulting in a unique cooperative effect.

3.5. Theoretical calculation

Theoretical calculations were conducted to study the electronic structure and charge density in KMO and HE-KMO. Fig. 5a, b shows the 2D charge density of HE-KMO and KMO. In contrast to the orderly electron cloud distribution in KMO, the influence of high-entropy doping leads to a disordered local electron cloud distribution in HE-KMO. Specifically, the Mn in HE-KMO is replaced by doping elements

(as shown, Mn is replaced by Ni and Fe). The electron clouds of the doping elements differ from those of the original Mn, disrupting the previously orderly Mn-O bond distribution. This results in the disruption of the long-range order inherent to KMO, transforming it into HE-KMO, which has local disorder [51,52]. Fig. 5c, d display the migration paths of potassium ions in the crystal cells of HE-KMO and KMO from different perspectives. Due to the influence of local disorder, potassium ions have different migration paths in HE-KMO compared to KMO. Fig. 5e calculated the diffusion barriers of K^+ along the migration paths in HE-KMO and KMO. We found that potassium ions in HE-KMO have a diffusion barrier of just 0.3, significantly lower than the 0.6 in KMO. This suggests that the local disorder of HE-KMO induces the transport of potassium ions, allowing them to migrate through more suitable paths, thus significantly reducing the energy barrier for potassium ion transport. Crystal Orbital Hamilton Population (COHP) can be used to understand the interactions between atoms. Positive and negative values in the COHP diagram represent anti-bonding and bonding interactions, respectively. As depicted in Fig. 5f, g, HE-KMO exhibits more complex bond interactions than KMO due to the incorporation of different elements. The integral COHP (ICOHP) at the Fermi level can serve as an indicator of bond strength. We integrated the Mn-O bond, and the Mn-O bond in HE-KMO has a value of 1.64, more significant than 1.32 in KMO. This indicates that HE-KMO has stronger bond energy and stability. As is widely recognized, interlayer sliding can occur in layered oxides during the charging and discharging process, leading to a decrease in material stability [53]. We computed the gliding energy barriers of KMO and HE-KMO with varying contents of K^+ , as shown in Fig. 5h. Regardless of the K^+ content, HE-KMO consistently exhibits a higher sliding barrier compared to KMO. This indicates that HE-KMO has superior structural stability during the process of potassium ion deintercalation.

3.6. Full cell performance

To demonstrate the practicality of HE-KMO, we assembled a full HE-KMO//PNTCDA cell with 1,4,5,8-naphthalenetetracarboxylic dianhydride-derived polyimide (PNTCDA) as the cathode. The mass ratio between PNTCDA and HE-KMO was 1.2:1. We tested the CV curves of PNTCDA half-cells at different scan rates and found that PNTCDA has a pair of redox peaks in 1 M KAC solution (Fig. 6a). The CV curve of the HE-KMO//PNTCDA full cell matches the redox peaks of both components, merging into a broader pair of redox peaks (Fig. 6b, c). We conducted charge-discharge tests on the full cell, and the rate performance plot of the full cell is shown in Fig. 6d, e, with the specific capacity decreasing as the current increases. When the current returns to 1 A g^{-1} , the specific capacity also returns to its original size. Moreover, when the full cell undergoes long cycling at 1 A g^{-1} , the material still maintains nearly 100% capacity after 1000 cycles (Fig. 6g). The curves of the 1st, 500th, and 1000th cycles, shown in (Fig. 6f), reveal that the curves remain similar even after multiple cycles. We compared the cycling performance of AKIBs reported in recent literature (Fig. 6h), and the HE-KMO//PNTCDA full cell exhibits excellent stability. This indicates the high-entropy doping strategy significantly improves the stability of HE-KMO, expanding the selection and applicability of aqueous potassium-ion battery materials.

4. Conclusion

In summary, we successfully synthesized high-entropy doped layered manganese oxide (HE-KMO) by doping Fe, Co, Ni, Zn, and Mg elements into layered manganese oxide (LMO). Multiple doped elements disturbed the distribution of the interlayer electron cloud in HE-KMO, leading to local disorder in HE-KMO. Local disorder induces potassium ions to disrupt their intrinsic transmission pathways, thus regulating their insertion. Through the regulation of potassium ions, local disorder lessens the severe stress changes that the material undergoes during the cycling process, curbs the distortion and dissolution issues related to the

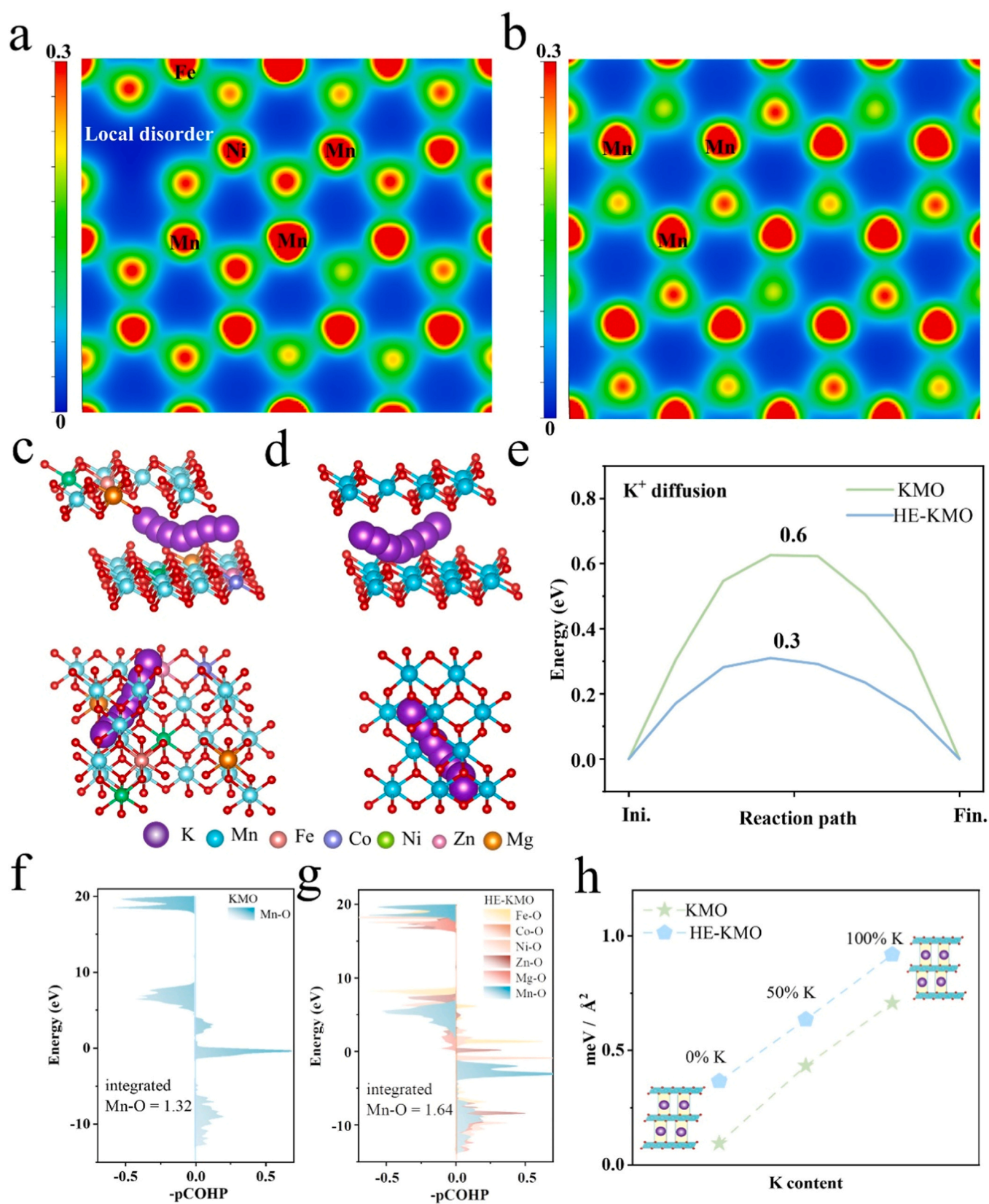


Fig. 5. Distribution of charge density for HE-KMO (a) and KMO (b) (visualized via VESTA). Front and top views of the K^+ migration path in the crystal cells of HE-KMO (c) and KMO (d). (e) Diffusion barrier of K^+ . (f,g) COHP diagrams of KMO and HE-KMO. (h) Gliding barriers of KMO and HE-KMO embedded with different ratios of potassium ions.

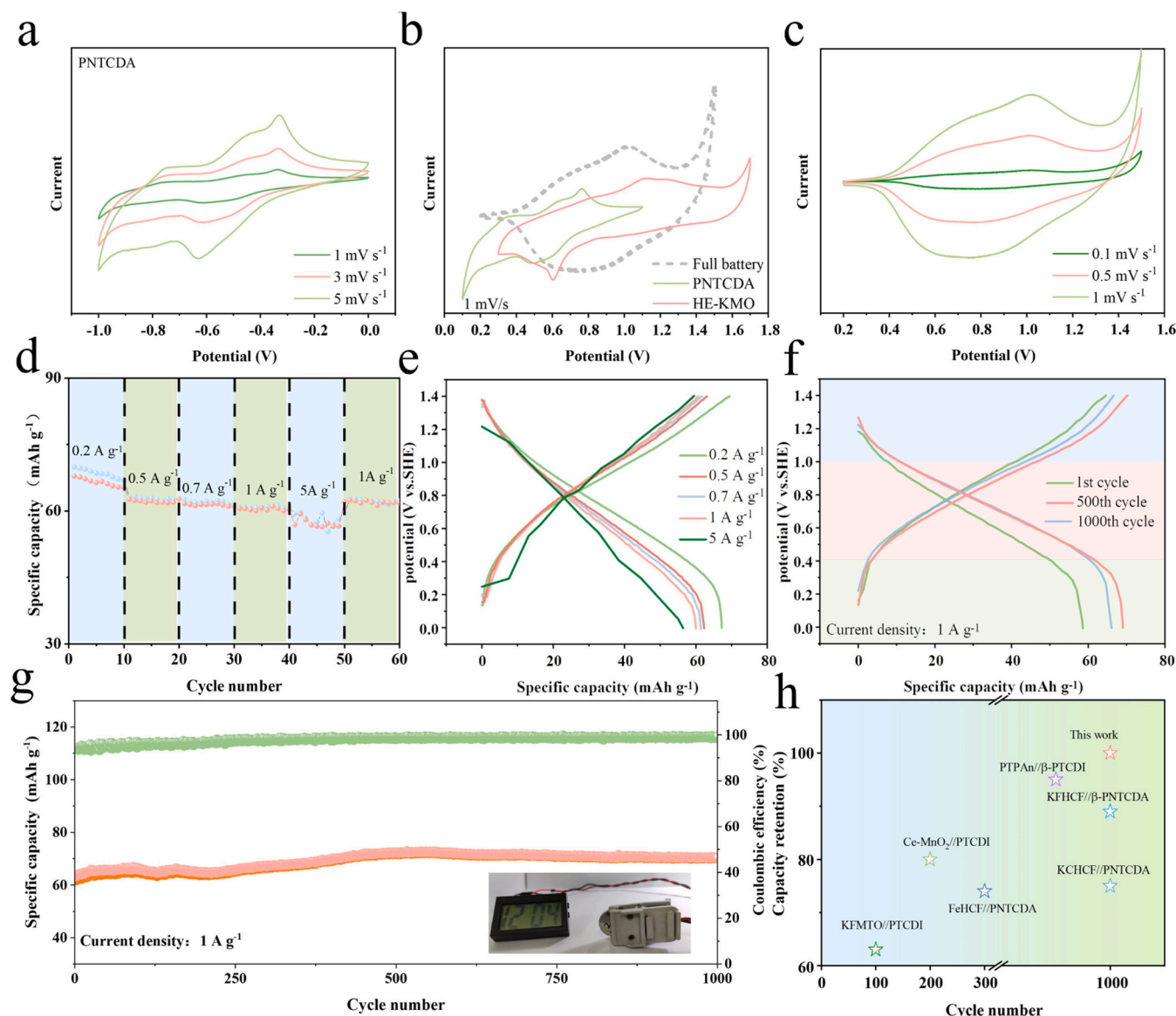


Fig. 6. (a) CV curves of PNTCDA with different sweep speeds. (b) Schematic diagram of CV for the full cell. (c) CV curves of the full cell with different sweep speeds. (d) Rate capability of the full cell from 0.2 to 5 A g⁻¹. (e) Full cell charge/discharge curves from 0.2 to 5 A g⁻¹. (f) Full cell charge/discharge curves for the 1st, 500th, and 1000th cycles at 1 A g⁻¹. (g) The full cell cycling stability for 500 cycles at 1 A g⁻¹ current density. (h) Cycling performance of the full cell [23,54–58].

material's lattice change, and notably lowers the energy barrier for potassium ion transport. This significantly enhances the stability of the material in aqueous potassium-ion batteries, preventing the material from rapidly dissolving in water. HE-KMO demonstrated excellent performance in aqueous potassium ion batteries. HE-KMO can sustain almost 100% capacity retention after 500 cycles. Moreover, in the HE-KMO//PNTCDA full cell, HE-KMO still showed excellent stability after 1000 cycles, higher than the stability of the previously reported aqueous potassium ion battery materials. The impressive stability of HE-KMO not only broadened the selection of positive electrode materials for AKIBs but also provided new insights for the improvement strategy of LMO materials.

CRediT authorship contribution statement

Maoyu Sun: Project administration. **Yiqian Li:** Formal analysis. **Hongfeng Jia:** Formal analysis. **Guowei Zeng:** Writing – review & editing, Writing – original draft, Methodology, Formal analysis, Data curation. **Bingqiu Liu:** Supervision, Funding acquisition, Formal

analysis. **Usman Ali:** Resources. **Yanxin Li:** Methodology. **Yuehan Hao:** Software. **Xue Yong:** Formal analysis. **Tingting Wang:** Supervision, Funding acquisition, Conceptualization. **Chungang Wang:** Resources, Data curation, Conceptualization.

Declaration of Competing Interest

The authors declare no competing interests.

Data availability

Data will be made available on request.

Acknowledgments

This work was supported by the National Natural Science Foundation of China (22172023, 22275031, 22375033 and 22305032), China Postdoctoral Science Foundation (2022M710653), the Jilin Provincial Research Foundation for Basic Research (20230101049JC), the

Fundamental Research Funds for the Central Universities (2412022XK012, 2412022QD006), Science and Technology Research project of the Education Department of Jilin Province (JJKH20220728KJ), The Science and Technology Project of Jilin Provincial Department of Education (JJKH20231299KJ), the natural science foundation of Chongqing, China (CSTB2022NSCQ-MSX0569).

Appendix A. Supporting information

Supplementary data associated with this article can be found in the online version at [doi:10.1016/j.apcatb.2024.123996](https://doi.org/10.1016/j.apcatb.2024.123996).

References

- [1] X. Min, J. Xiao, M. Fang, W. Wang, Y. Zhao, Y. Liu, A.M. Abdelkader, K. Xi, R. V. Kumar, Z. Huang, Potassium-ion batteries: outlook on present and future technologies, *Energy Environ. Sci.* 14 (4) (2021) 2186–2243, <https://doi.org/10.1039/D0EE02917C>.
- [2] S. Chu, A. Majumdar, Opportunities and challenges for a sustainable energy future, *Nature* 488 (7411) (2012) 294–303, <https://doi.org/10.1038/nature11475>.
- [3] B. Dunn, H. Kamath, J.-M. Tarascon, Electrical energy storage for the grid: a battery of choices, *Sci.* 334 (6058) (2011) 928–935, <https://doi.org/10.1126/science.1212741>.
- [4] H. Liang, Z. Gai, F. Chen, S. Jing, W. Kan, B. Zhao, S. Yin, P. Tsiakaras, Fe₃C decorated wood-derived integral N-doped C cathode for rechargeable Li-O₂ batteries, *Appl. Catal. B Environ.* 324 (2023) 122203, <https://doi.org/10.1016/j.apcatb.2022.122203>.
- [5] K. Liivand, J. Sainio, B.P. Wilson, I. Kruusenberg, M. Lundström, Overlooked residue of Li-ion battery recycling waste as high-value bifunctional oxygen electrocatalyst for Zn-air batteries, *Appl. Catal. B Environ.* 332 (2023) 122767, <https://doi.org/10.1016/j.apcatb.2023.122767>.
- [6] E.Y. Choi, D.E. Kim, S.Y. Lee, C.B. Park, C.K. Kim, Cobalt nanoparticles-encapsulated holey nitrogen-doped carbon nanotubes for stable and efficient oxygen reduction and evolution reactions in rechargeable Zn-air batteries, *Appl. Catal. B Environ.* 325 (2023) 122386, <https://doi.org/10.1016/j.apcatb.2023.122386>.
- [7] C. Lai, M. Gong, Y. Zhou, J. Fang, L. Huang, Z. Deng, X. Liu, T. Zhao, R. Lin, K. Wang, K. Jiang, H. Xin, D. Wang, Sulphur modulated Ni₃FeN supported on N/S co-doped graphene boosts rechargeable/flexible Zn-air battery performance, *Appl. Catal. B Environ.* 274 (2020) 119086, <https://doi.org/10.1016/j.apcatb.2020.119086>.
- [8] B. Liu, Q. Zhang, Y. Li, Y. Hao, U. Ali, L. Li, L. Zhang, C. Wang, Z. Su, Realizing complete solid-solution reaction to achieve temperature independent LiFePO₄ for high rate and low temperature Li-Ion batteries, *CCS Chem.* 5 (1) (2023) 209–220, <https://doi.org/10.31635/ccschem.022.202201776>.
- [9] Y.-F. Meng, H.-J. Liang, C.-D. Zhao, W.-H. Li, Z.-Y. Gu, M.-X. Yu, B. Zhao, X.-K. Hou, X.-L. Wu, Concurrent recycling chemistry for cathode/anode in spent graphite/LiFePO₄ batteries: designing a unique cation/anion-co-workable dual-ion battery, *J. Energy Chem.* 64 (2022) 166–171, <https://doi.org/10.1016/j.jechem.2021.04.047>.
- [10] H.-J. Liang, Z.-Y. Gu, X.-X. Zhao, J.-Z. Guo, J.-L. Yang, W.-H. Li, B. Li, Z.-M. Liu, Z.-H. Sun, J.-P. Zhang, X.-L. Wu, Advanced flame-retardant electrolyte for highly stabilized K-ion storage in graphite anode, *Sci. Bull.* 67 (15) (2022) 1581–1588, <https://doi.org/10.1016/j.scib.2022.07.002>.
- [11] J. Huang, Z. Wang, M. Hou, X. Dong, Y. Liu, Y. Wang, Y. Xia, Polyaniline-intercalated manganese dioxide nanolayers as a high-performance cathode material for an aqueous zinc-ion battery, *Nat. Commun.* 9 (1) (2018) 2906, <https://doi.org/10.1038/s41467-018-04949-4>.
- [12] H. Jia, Y. Li, U. Ali, Y. Li, Y. Hao, B. Liu, C. Wang, L. Li, H.-g. Wang, In-situ formation of ultrafine ZnMn₂O₄-MnOOH composite nanoparticles embedded into porous carbon nanospheres for stable aqueous zinc-ion batteries, *Appl. Surf. Sci.* 592 (2022) 153279, <https://doi.org/10.1016/j.apsusc.2022.153279>.
- [13] F. Bu, Z. Sun, W. Zhou, Y. Zhang, Y. Chen, B. Ma, X. Liu, P. Liang, C. Zhong, R. Zhao, H. Li, L. Wang, T. Zhang, B. Wang, Z. Zhao, J. Zhang, W. Li, Y.S. Ibrahim, Y. Hassan, A. Elzatabry, D. Chao, D. Zhao, Reviving ZnO dendrites to electroactive Zn²⁺ by mesoporous mxene with active edge sites, *J. Am. Chem. Soc.* 145 (44) (2023) 24284–24293, <https://doi.org/10.1021/jacs.3c08986>.
- [14] Z. Hou, T. Zhang, X. Liu, Z. Xu, J. Liu, W. Zhou, Y. Qian, H.J. Fan, D. Chao, D. Zhao, A solid-to-solid metallic conversion electrochemistry toward 91% zinc utilization for sustainable aqueous batteries, *Science Advances* 8(41) eabp8960, <https://doi.org/10.1126/sciadv.abp8960>.
- [15] Z. Yang, B. Wang, Y. Chen, W. Zhou, H. Li, R. Zhao, X. Li, T. Zhang, F. Bu, Z. Zhao, W. Li, D. Chao, D. Zhao, Activating sulfur oxidation reaction via six-electron redox mesocrystal NiS₂ for sulfur-based aqueous batteries, *Natl. Sci. Rev.* 10 (6) (2023) nwac268, <https://doi.org/10.1093/nsr/nwac268>.
- [16] Y. Cai, X. Zeng, D. Pang, Y. Gu, J. Qi, T. Masese, F. Chang, Y. Li, S. Wang, Z. Li, Z.-D. Huang, Layered transition metal oxides prepared by plasma-enhanced sintering technique as environmentally stable cathode for potassium-ion batteries, *Materialia* 27 (2023) 101674, <https://doi.org/10.1016/j.mtla.2023.101674>.
- [17] P. Luo, Z. Huang, W. Zhang, C. Liu, G. Liu, M. Huang, Y. Xiao, H. Luo, Z. Qu, S. Dong, L. Xia, H. Tang, Q. An, Incorporating near-pseudocapacitance insertion Ni/Co-based hexacyanoferrate and low-cost metallic Zn for aqueous k-ion batteries, *ChemSusChem* 15 (16) (2022) e202200706, <https://doi.org/10.1002/cssc.202200706>.
- [18] H. Liu, J. Zhang, X. Zhang, J. Li, Y. Liu, X. Cai, W. Li, H. Yu, L. Yan, L. Zhang, J. Shu, Cobalt hexacyanoferrate enhanced by common ion effect for aqueous potassium-ion batteries, *Appl. Surf. Sci.* 604 (2022) 154654, <https://doi.org/10.1016/j.apsusc.2022.154654>.
- [19] J. Han, A. Mariani, H. Zhang, M. Zarrabaitia, X. Gao, D.V. Carvalho, A. Varzi, S. Passerini, Gelified acetate-based water-in-salt electrolyte stabilizing hexacyanoferrate cathode for aqueous potassium-ion batteries, *Energy Storage Mater.* 30 (2020) 196–205, <https://doi.org/10.1016/j.ensm.2020.04.028>.
- [20] Z. Sun, Y. Chen, C. Geng, Y. Li, W. Guo, J. Jiang, Y. Cui, Y. Shi, Q. Zhuang, Z. Ju, Oxygen-driven bulk defect engineering in carbon to reduce voltage hysteresis for fast potassium storage at low voltage, *Appl. Catal. B Environ.* 343 (2024) 123473, <https://doi.org/10.1016/j.apcatb.2023.123473>.
- [21] X. Yi, Y. Feng, A.M. Rao, J. Zhou, C. Wang, B. Lu, Quasi-solid aqueous electrolytes for low-cost sustainable alkali-metal batteries, *Adv. Mater.* 35 (29) (2023) 2302280, <https://doi.org/10.1002/adma.202302280>.
- [22] H. Ding, J. Wang, J. Zhou, C. Wang, B. Lu, Building electrode skins for ultra-stable potassium metal batteries, *Nat. Commun.* 14 (1) (2023) 2305, <https://doi.org/10.1038/s41467-023-38065-9>.
- [23] G. Zeng, U. Ali, M. Sun, Y. Zhang, L. Fu, Y. Li, Y. Hao, B. Liu, C. Wang, Intercalation pseudocapacitance mechanism realizes high-performance cathode for aqueous potassium ion batteries, *J. Colloid Interface Sci.* 653 (2024) 46–55, <https://doi.org/10.1016/j.jcis.2023.09.061>.
- [24] T. Masese, K. Yoshii, Y. Yamaguchi, T. Okumura, Z.-D. Huang, M. Kato, K. Kubota, J. Furutani, Y. Orikasa, H. Senoh, H. Sakaebae, M. Shikano, Rechargeable potassium-ion batteries with honeycomb-layered tellurates as high voltage cathodes and fast potassium-ion conductors, *Nat. Commun.* 9 (1) (2018) 3823, <https://doi.org/10.1038/s41467-018-06343-6>.
- [25] Z. Li, J. Wen, Y. Cai, F. Lv, X. Zeng, Q. Liu, T. Masese, C. Zhang, X. Yang, Y. Ma, H. Zhang, Z.-D. Huang, Hydrated Bi-Ti-bimetal ethylene glycol: a new high-capacity and stable anode material for potassium-ion batteries, *Adv. Funct. Mater.* 33 (22) (2023) 2300582, <https://doi.org/10.1002/adfm.202300582>.
- [26] J. Wu, B. Yuan, Y. Gu, Y. Zhang, Z. Yan, L. Zhang, X. Yang, H. Zhang, L. Bai, Z. Li, Z.-D. Huang, Multifunctional layered bismuth oxychloride/amorphous antimony oxide hetero-hybrids as superior photocatalyst and potassium ion storage materials, *Appl. Catal. B Environ.* 321 (2023) 122032, <https://doi.org/10.1016/j.apcatb.2022.122032>.
- [27] J. Chen, B. Luo, Q. Chen, F. Li, Y. Guo, T. Wu, P. Peng, X. Qin, G. Wu, M. Cui, L. Liu, L. Chu, B. Jiang, Y. Li, X. Gong, Y. Chai, Y. Yang, Y. Chen, W. Huang, X. Liu, M. Li, Localized electrons enhanced ion transport for ultrafast electrochemical energy storage, *Adv. Mater.* 32 (14) (2020) 1905578, <https://doi.org/10.1002/adma.201905578>.
- [28] Z. Cai, S. Wang, H. Zhu, X. Tang, Y. Ma, D.Y.W. Yu, S. Zhang, G. Song, W. Yang, Y. Xu, C. Wen, Improvement of stability and capacity of Co-free, Li-rich layered oxide Li_{1.2}Ni_{0.2}Mn_{0.6}O₂ cathode material through defect control, *J. Colloid Interface Sci.* 630 (2023) 281–289, <https://doi.org/10.1016/j.jcis.2022.10.105>.
- [29] N. Li, M. Sun, W.H. Kan, Z. Zhuo, S. Hwang, S.E. Renfrew, M. Avdeev, A. Huq, B. D. McCloskey, D. Su, W. Yang, W. Tong, Layered-rocksalt intergrown cathode for high-capacity zero-strain battery operation, *Nat. Commun.* 12 (1) (2021) 2348, <https://doi.org/10.1038/s41467-021-22527-z>.
- [30] Y. Ma, P. Liu, Q. Xie, G. Zhang, H. Zheng, Y. Cai, Z. Li, L. Wang, Z.-Z. Zhu, L. Mai, D.-L. Peng, Double-shell Li-rich layered oxide hollow microspheres with sandwich-like carbon@spinel@layered@spinel@carbon shells as high-rate lithium ion battery cathode, *Nano Energy* 59 (2019) 184–196, <https://doi.org/10.1016/j.nanoen.2019.02.040>.
- [31] M. Reynaud, J. Serrano-Sevillano, M. Casas-Cabanas, Imperfect battery materials: a closer look at the role of defects in electrochemical performance, *Chem. Mater.* 35 (9) (2023) 3345–3363, <https://doi.org/10.1021/acs.chemmater.2c03481>.
- [32] Y. Li, H. Jia, U. Ali, H. Wang, B. Liu, L. Li, L. Zhang, C. Wang, Successive gradient internal electric field strategy toward dendrite-free zinc metal anode, *Adv. Energy Mater.* (2023) 2301643, <https://doi.org/10.1002/aenm.202301643>.
- [33] M.P. Stockham, B. Dong, M.S. James, P. Zhu, E. Kendrick, P.R. Slater, Rapid sintering of Li_{6.5}La₃Zr₁Nb_{0.5}Ce_{0.25}Ti_{0.25}O₁₂ for high density lithium garnet electrolytes with current induced in situ interfacial resistance reduction, *Energy Adv.* 2 (10) (2023) 1660–1673, <https://doi.org/10.1039/D3YA00123G>.
- [34] Y. Zeng, B. Ouyang, J. Liu, Y.-W. Byeon, Z. Cai, L.J. Miara, Y. Wang, G. Ceder, High-entropy mechanism to boost ionic conductivity, *Science* 378 (6626) (2022) 1320–1324, <https://doi.org/10.1126/science.abq1346>.
- [35] J. Ma, C. Huang, High entropy energy storage materials: synthesis and application, *J. Energy Storage* 66 (2023) 107419, <https://doi.org/10.1016/j.est.2023.107419>.
- [36] Y. Cai, W. Liu, F. Chang, S. Jin, X. Yang, C. Zhang, L. Bai, T. Masese, Z. Li, Z.-D. Huang, Entropy-stabilized layered K_{0.6}Ni_{0.05}Fe_{0.05}Mg_{0.05}Ti_{0.05}Mn_{0.725}O₂ as a high-rate and stable cathode for potassium-ion batteries, *ACS Appl. Mater. Interfaces* (2023), <https://doi.org/10.1021/acsami.3c11059>.
- [37] J. Wang, Y. Cui, Q. Wang, K. Wang, X. Huang, D. Stenzel, A. Sarkar, R. Azmi, T. Bergfeldt, S.S. Bhattacharya, R. Kruk, H. Hahn, S. Schweidler, T. Brezesinski, B. Breitling, Lithium containing layered high entropy oxide structures, *Sci. Rep.* 10 (1) (2020) 18430, <https://doi.org/10.1038/s41598-020-75134-1>.
- [38] S. Li, L. Wu, H. Fu, A.M. Rao, L. Cha, J. Zhou, B. Lu, Entropy-tuned layered oxide cathodes for potassium-ion batteries, *Small Methods* (2023) 2300893, <https://doi.org/10.1002/smt.202300893>.
- [39] R. Zhang, C. Wang, P. Zou, R. Lin, L. Ma, L. Yin, T. Li, W. Xu, H. Jia, Q. Li, S. Sainio, K. Kisslinger, S.E. Trask, S.N. Ehrlich, Y. Yang, A.M. Kiss, M. Ge, B.J. Polzin, S. J. Lee, W. Xu, Y. Ren, H.L. Xin, Compositionally complex doping for zero-strain

- zero-cobalt layered cathodes, *Nature* 610 (7930) (2022) 67–73, <https://doi.org/10.1038/s41586-022-05115-z>.
- [40] Q. Shen, X. Zhao, Y. Liu, Y. Li, J. Zhang, N. Zhang, C. Yang, J. Chen, Dual-strategy of cation-doping and nanoengineering enables fast and stable sodium-ion storage in a novel Fe/Mn-based layered oxide cathode, *Adv. Sci.* 7 (21) (2020) 2002199, <https://doi.org/10.1002/advs.202002199>.
- [41] Z.-Y. Gu, J.-Z. Guo, J.-M. Cao, X.-T. Wang, X.-X. Zhao, X.-Y. Zheng, W.-H. Li, Z.-H. Sun, H.-J. Liang, X.-L. Wu, An advanced high-entropy fluorophosphate cathode for sodium-ion batteries with increased working voltage and energy density, *Adv. Mater.* 34 (14) (2022) 2110108, <https://doi.org/10.1002/adma.202110108>.
- [42] Z.-Y. Li, X. Ma, H. Guo, L. He, Y. Li, G. Wei, K. Sun, D. Chen, Complementary effect of Ti and Ni incorporation in improving the electrochemical performance of a layered sodium manganese oxide cathode for sodium-ion batteries, *ACS Appl. Energy Mater.* 4 (6) (2021) 5687–5696, <https://doi.org/10.1021/acsami.1c00527>.
- [43] Y. Xu, G. Zhang, J. Zhang, X. Wang, J. Wang, S. Jia, Y. Yuan, X. Yang, K. Xu, C. Wang, K. Zhang, W. Li, X. Li, Oxygen vacancies in MnO_x regulating reaction kinetics for aqueous zinc-ion batteries, *J. Colloid Interface Sci.* 652 (2023) 305–316, <https://doi.org/10.1016/j.jcis.2023.08.084>.
- [44] B. Pandit, S.R. Rondiya, N.Y. Dzade, S.F. Shaikh, N. Kumar, E.S. Goda, A.A. Al-Kahtani, R.S. Mane, S. Mathur, R.R. Salunkhe, High stability and long cycle life of rechargeable sodium-ion battery using manganese oxide cathode: a combined density functional theory (DFT) and experimental study, *ACS Appl. Mater. Interfaces* 13 (9) (2021) 11433–11441, <https://doi.org/10.1021/acsami.0c21081>.
- [45] F. Wu, X. Gao, X. Xu, Y. Jiang, X. Gao, R. Yin, W. Shi, W. Liu, G. Lu, X. Cao, MnO_2 Nanosheet-assembled hollow polyhedron grown on carbon cloth for flexible aqueous zinc-ion batteries, *ChemSusChem* 13 (6) (2020) 1537–1545, <https://doi.org/10.1002/cssc.201903006>.
- [46] A. Li, C. Li, P. Xiong, J. Zhang, D. Geng, Y. Xu, Rapid synthesis of layered K_xMnO_2 cathodes from metal–organic frameworks for potassium-ion batteries, *Chem. Sci.* 13 (25) (2022) 7575–7580, <https://doi.org/10.1039/D2SC02442J>.
- [47] M.K. Cho, J.H. Jo, J.U. Choi, S.-T. Myung, Cycling Stability of layered potassium manganese oxide in nonaqueous potassium cells, *ACS Appl. Mater. Interfaces* 11 (31) (2019) 27770–27779, <https://doi.org/10.1021/acsami.9b06915>.
- [48] Y. Sun, S. Guo, H. Zhou, Adverse effects of interlayer-gliding in layered transition-metal oxides on electrochemical sodium-ion storage, *Energy Environ. Sci.* 12 (3) (2019) 825–840, <https://doi.org/10.1039/C8EE01006D>.
- [49] B. Xiao, Y. Wang, S. Tan, M. Song, X. Li, Y. Zhang, F. Lin, K.S. Han, F. Omenya, K. Amine, X.-Q. Yang, D. Reed, Y. Hu, G.-L. Xu, E. Hu, X. Li, X. Li, Vacancy-enabled O_3 phase stabilization for manganese-rich layered sodium cathodes, *Angew. Chem. Int. Ed.* 60 (15) (2021) 8258–8267, <https://doi.org/10.1002/anie.202016334>.
- [50] B. Liu, Q. Zhang, U. Ali, Y. Li, Y. Hao, L. Zhang, Z. Su, L. Li, C. Wang, Solid-solution reaction suppresses the Jahn–teller effect of potassium manganese hexacyanoferrate in potassium-ion batteries, *Chem. Sci.* 13 (36) (2022) 10846–10855, <https://doi.org/10.1039/D2SC03824B>.
- [51] B. Liu, Q. Zhang, L. Zhang, X. Yong, L. Li, C. Wang, Manganese charge redistribution induced by high-entropy charge compensation mechanism for aqueous potassium-ion batteries, *Energy Storage Mater.* 66 (2024) 103221, <https://doi.org/10.1016/j.ensm.2024.103221>.
- [52] H. Jia, Y. Li, U. Ali, B. Liu, Z. Jin, L. Li, Y. Chen, L. Zhang, T. Wang, C. Wang, High-entropy doping strategy towards reinforced Mn–O bond for durable aqueous zinc ion batteries, *Nano Energy* 122 (2024) 109348, <https://doi.org/10.1016/j.nanoen.2024.109348>.
- [53] M. Sadowski, L. Koch, K. Albe, S. Siculo, Planar gliding and vacancy condensation: the role of dislocations in the chemomechanical degradation of layered transition-metal oxides, *Chem. Mater.* 35 (2) (2023) 584–594, <https://doi.org/10.1021/acs.chemmater.2c03069>.
- [54] X. Zhang, X. Yang, G. Sun, S. Yao, Y. Xie, W. Zhang, C. Liu, X. Wang, R. Yang, X. Jin, Z.X. Shen, H.J. Fan, F. Du, Hydration enables air-stable and high-performance layered cathode materials for both organic and aqueous potassium-ion batteries, *Adv. Funct. Mater.* 32 (41) (2022) 2204318, <https://doi.org/10.1002/adfm.202204318>.
- [55] M. Wang, H. Wang, H. Zhang, X. Li, Aqueous K-ion battery incorporating environment-friendly organic compound and berlin green, *J. Energy Chem.* 48 (2020) 14–20, <https://doi.org/10.1016/j.jechem.2019.12.019>.
- [56] U. Ali, B. Liu, H. Jia, Y. Li, Y. Li, Y. Hao, L. Zhang, S. Xing, L. Li, C. Wang, In situ Fe-substituted hexacyanoferrate for high-performance aqueous potassium ion batteries, *Small* (2023) 2305866, <https://doi.org/10.1002/sml.202305866>.
- [57] H. Chen, Z. Zhang, Z. Wei, G. Chen, X. Yang, C. Wang, F. Du, Use of a water-in-salt electrolyte to avoid organic material dissolution and enhance the kinetics of aqueous potassium ion batteries, *Sustain. Energy Fuels* 4 (1) (2020) 128–131, <https://doi.org/10.1039/C9SE00545E>.
- [58] J. Ge, X. Yi, L. Fan, B. Lu, An all-organic aqueous potassium dual-ion battery, *J. Energy Chem.* 57 (2021) 28–33, <https://doi.org/10.1016/j.jechem.2020.08.049>.